Single- and Multimagnon Dynamics in Antiferromagnetic α-Fe$_2$O$_3$ Thin Films

Jiemin Li[1,*], Yanhong Gu,[1] Yoshihiro Takahashi,[2] Keisuke Higashi,[2] Taehun Kim[1], Yang Cheng,[3]
Fengyuan Yang,[3] Jan Kuneš[4], Jonathan Pelliciari[1], Atsushi Hariki[2], and Valentina Bisogni[1,†]

[1]*National Synchrotron Light Source II, Brookhaven National Laboratory, Upton, New York 11973, USA*
[2]*Department of Physics and Electronics, Osaka Metropolitan University,*
1-1 Gakuen-cho, Nakaku, Sakai, Osaka 599-8531, Japan
[3]*Department of Physics, The Ohio State University, Columbus, Ohio 43210, USA*
[4]*Institute of Solid State Physics, TU Wien, 1040 Vienna, Austria*

Understanding the spin dynamics in antiferromagnetic (AFM) thin films is fundamental for designing novel devices based on AFM magnon transport. Here, we study the magnon dynamics in thin films of AFM $S = \frac{5}{2}$ α-Fe$_2$O$_3$ by combining resonant inelastic x-ray scattering, Anderson impurity model plus dynamical mean-field theory, and Heisenberg spin model. Below 100 meV, we observe the thickness-independent (down to 15 nm) acoustic single-magnon mode. At higher energies (100–500 meV), an unexpected sequence of equally spaced, optical modes is resolved and ascribed to $\Delta S_z = 1, 2, 3, 4$, and 5 magnetic excitations corresponding to multiple, noninteracting magnons. Our study unveils the energy, character, and momentum dependence of single and multimagnons in α-Fe$_2$O$_3$ thin films, with impact on AFM magnon transport and its related phenomena. From a broader perspective, we generalize the use of L-edge resonant inelastic x-ray scattering as a multispin-excitation probe up to $\Delta S_z = 2S$. Our analysis identifies the spin-orbital mixing in the valence shell as the key element for accessing excitations beyond $\Delta S_z = 1$, and up to, e.g., $\Delta S_z = 5$. At the same time, we elucidate the novel origin of the spin excitations beyond the $\Delta S_z = 2$, emphasizing the key role played by the crystal lattice as a reservoir of angular momentum that complements the quanta carried by the absorbed and emitted photons.

Subject Areas: Condensed Matter Physics

I. INTRODUCTION

The never-ending demand for faster and low-power devices is stimulating the development of novel electronics such as antiferromagnetic spintronics [1,2]. In this context, insulating antiferromagnets are highly attractive as they support novel spin-transport phenomena conveyed by AFM magnons [3,4] without involving moving charges. As a result, renewed interest is now focused on well-known AFM materials, such as α-Fe$_2$O$_3$ (hematite) which offers functional opportunities including long-distance spin transport [5–7] and electrical switching of the Néel order [8–11]. Hence, to progress in AFM spintronics, magnon transport, and its underlying microscopic phenomena, it is crucial to understand the whole magnon spectrum, i.e., single and

multimagnons, in thin-film form as used for devices. Indeed, thin films often present deviations in the spin q-dynamics with respect to the bulk, owing to strain, confinement, electronic band reconstruction, etc. [12–15].

Only limited information is, however, available on magnon dynamics in thin films, mostly due to lack of suitable experimental probes. Thanks to dramatic improvements in the energy resolution, resonant inelastic x-ray scattering (RIXS) is emerging as a powerful tool for the study of spin dynamics in magnetic materials [16–25] and in thin films [14,26,27]. Concomitantly, relevant progress in the theoretical description of the RIXS process contributed to elucidate the complex magnetic interactions behind the RIXS cross section [17,28–32]. As an example, a unique sensitivity to multispin excitations up to $\Delta S_z = 2$ was revealed [22,33–36], contrary to conventional magnon probes. Therefore, this novel approach promises to bridge the present gap in the study of single and multimagnons in thin film and bulk materials.

Here, we focus on $S = \frac{5}{2}$ α-Fe$_2$O$_3$ aiming to investigate the magnon modes and their q-dynamics in 30- and 15-nm thin films by using high-resolution Fe L_3-edge RIXS. Below 100 meV, the dispersing single-magnon mode revealed in

*jli1@bnl.gov
†bisogni@bnl.gov

the two thin films perfectly match each other as well as the same mode in the bulk [37–39]. At higher energies, our data instead displays unexpected, equally spaced peaks in the approximately (100–500)-meV range with negligible q-dependence. Combining the Anderson impurity model (AIM) built on local density approximation (LDA) plus dynamical mean-field theory (DMFT) and Heisenberg model analysis, we demonstrate these modes to be magnetic and noninteracting, corresponding to $\Delta S_z = 1, 2, 3, 4$, and 5 multimagnon excitations. Overall, our study provides information on the fundamental magnetic modes in hematite thin films, which are of relevance, e.g., for magnon transport and pumping phenomena. At the same time, we highlight L-edge RIXS as an effective method for accessing multimagnon excitations. Thanks to an analysis of the spin character during the intermediate state, we identify the spin-orbital mixing in the valence shell as the key element for accessing magnons beyond $\Delta S_z = 1$ and up to $\Delta S_z = 2S$. We also demonstrate that the lattice-breaking spherical symmetry plays a crucial role in accessing $\Delta S_z > 2$, effectively acting as a reservoir for angular momentum.

II. EXPERIMENT DETAILS

High-quality crystalline thin films of α-Fe$_2$O$_3$ with 30 and 15 nm thickness are grown fully relaxed on Al$_2$O$_3$ [10], realizing the typical hematite corundum structure (see Sec. I of the Supplemental Material [40] for further details). The spin momentum $S = \frac{5}{2}$ deriving from the $3d^5$ high-spin electronic configuration of the Fe^{3+} ions [see inset of Fig. 1(b)] lies in the (001) plane and stacks antiferromagnetically along the c axis of the hexagonal cell; see Fig. 1(a).

Fe L_3-edge x-ray absorption spectroscopy (XAS) and RIXS measurements are performed at the SIX 2-ID beamline of the National Synchrotron Light Source II [41]. The RIXS experiment is conducted with an energy resolution of $\Delta E \sim 23$ meV (full width at half maximum) at the Fe L_3 edge. Linear-horizontal (π) polarization of the incident light is used to minimize the elastic scattering in the RIXS spectra. The films are oriented with the [120] and [001] axes lying in the scattering plane; see Fig. 1(a). The temperature is kept at $T = 100$ K. The momentum q
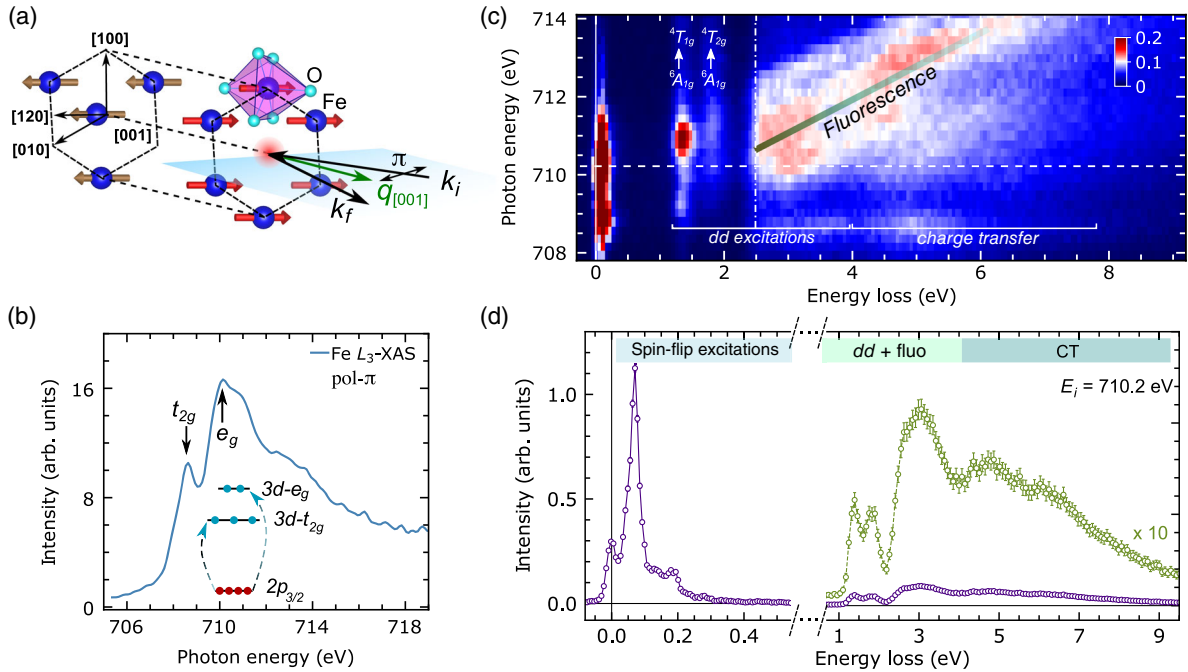

FIG. 1. Scattering geometry and experimental data for 30-nm α-Fe$_2$O$_3$ film. (a) Crystal and magnetic structure of α-Fe$_2$O$_3$. The blue shaded area indicates the scattering plane defined by the [001] and [120] axes of the hexagonal unit cell. The black arrows labeled k_i (k_f) represent the incident (scattered) x rays, while the double arrow refers to the π polarization. The momentum transfer q (green arrow) is along the [001] direction. (b) Fe L_3-edge XAS measured in the PFY mode using the RIXS spectrometer at Fe L_3 edge, $\theta = 33.5°$ and $2\theta = 67°$. The inset depicts the related Fe L_3 XAS process. XAS in total fluorescence or electron yield mode cannot be successfully measured in this sample due to technical difficulties. (c) RIXS energy dependence across the Fe L_3 edge at $\theta = 20°$ and $2\theta = 150°$, and π-polarized x rays. The horizontal dashed line indicates the incident photon energy 710.2 eV used for RIXS measurements, while the vertical dot-dashed line specifies the onset of fluorescence. (d) Overview of a typical high-resolution RIXS spectrum in purple color ($\theta = 45°$, $2\theta = 90°$, and $q = 0.51$ Å^{-1}). The high-energy-loss excitations are multiplied by a factor of 10 in the green colored spectrum to ease the visualization of the dd, charge transfer, and fluorescence fine structure. The error bars are defined assuming a Poisson distribution of the centroided, single-photon events.

transferred during the RIXS measurements is parallel to the [001] axis and defined in absolute unit Å^{-1}.

III. MAGNETIC EXCITATIONS OF $\alpha\text{-Fe}_2\text{O}_3$ FILMS

Figure 1(b) shows the Fe L_3-edge XAS of 30-nm $\alpha\text{-Fe}_2\text{O}_3$ film measured in partial fluorescence yield (PFY) mode. As the octahedral crystal field splits the Fe $3d$ orbitals into t_{2g} and e_g levels, the XAS peak at 708.8 eV (710.2 eV) corresponds to the transition from the $2p_{3/2}$ orbitals to the t_{2g} (e_g) ones [42], as illustrated in the inset of Fig. 1(b).

Figure 1(c) presents the energy dependence of the RIXS spectra across the Fe L_3 edge in the same sample. The color map reveals pronounced excitations in two well-separated energy-loss windows, respectively, below 500 meV and above 1 eV. In the latter case, we observe interorbital, Raman-like, dd excitations in the energy range of 1–4 eV, with two main branches emerging at approximately 1.4 and 1.9 eV. These dd excitations correspond to $^6A_{1g} \rightarrow {}^4T_{1g}$ and $^6A_{1g} \rightarrow {}^4T_{2g}$ transitions, flipping both spin ($S = \frac{5}{2} \rightarrow \frac{3}{2}$) and orbital ($e_g \rightarrow t_{2g}$), respectively. At higher energies, weak charge-transfer excitations involving the electron hopping between Fe $3d$ and O $2p$ orbitals start from approximately 4-eV energy loss and extend up to 10 eV. Furthermore, when the photon energy approaches the Fe e_g resonance [dashed line in Fig. 1(c)], a strong fluorescence emerges around 2.5 eV, shifting linearly in energy loss as the incident photon energy increases. Overall, the broad high-energy excitations discussed above are consistent with previous low-resolution RIXS studies of $\alpha\text{-Fe}_2\text{O}_3$ [31,43,44].

To introduce the low-energy excitations (below 500 meV), we display in Fig. 1(d) a representative high-resolution RIXS spectrum recorded at the Fe e_g resonance as it maximizes the intensity of the excitations below 100 meV (see Fig. S1 and Sec. II in the Supplemental Material [40]). The so far unresolved low-energy range of the hematite RIXS spectrum reveals multiple sharp excitations with the mode at approximately 100 meV appearing as resolution limited and dominating the overall spectral weight. Similar low-energy features with identical energies and intensities are observed in the 15-nm $\alpha\text{-Fe}_2\text{O}_3$ film in the same scattering conditions. The corresponding results are presented in Fig. S2 and Sec. III of the Supplemental Material [40].

As the main scope of this work is about the nature of these low-energy excitations, we present in Fig. 2(a) a closer view of the RIXS spectrum introduced in Fig. 1(d). A long sequence of excitations extending up to 500 meV is observed. Note that the intensity of the region between 200 and 500 meV is expanded by a factor of 15 for clarity. While it is known that magnon modes below 100 meV [38] and (multi) phonon modes up to 200 meV [45,46] exist in hematite, the richness of the excitations observed in the
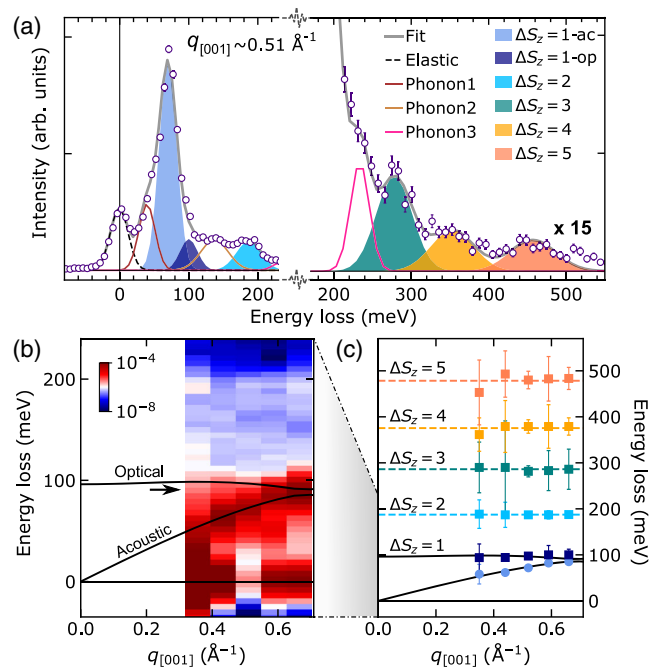

FIG. 2. Momentum dependence of low-energy excitations in 30-nm $\alpha\text{-Fe}_2\text{O}_3$ film. (a) Enlarged view of the selected RIXS spectrum in Fig. 1(c) at $q = 0.51$ Å^{-1} (open dots). The low-energy excitations up to 500 meV are fitted with ten Gaussians, as explained in the main text. The gray solid line is the sum of the fitted components. (b) RIXS color map (in logarithmic scale) as a function of q. The spectra are normalized to the integrated spectral weight in the region 0.6–8.0 eV. The black lines display the calculated single-magnon acoustic and optical branches for $\alpha\text{-Fe}_2\text{O}_3$ single crystal [38]. (c) Fitting results in terms of peak position versus q for the six unconstrained solid-filled Gaussians. The black lines are the same as in (b) and the color code is the same as in (a). The fit error bar is defined in Sec. V of the Supplemental Material [40].

RIXS data up to 500 meV is unprecedented. To scrutinize the origin of these modes, we conduct a momentum-dependent study, with q along the out-of-plane [001] direction. The result is displayed in Fig. 2(b) for energy losses up to 220 meV. A peak is observed dispersing upward in energy loss for increasing q and reaching approximately 100 meV at the zone boundary. Additional peaks with small or no momentum dependence are visible in the (100–200)-meV region of Fig. 2(b). Because of the weaker intensity of the latter excitations with respect to the ones below 100 meV, we fit all contributions in the RIXS spectra within the $(-100, 570)$-meV range to extract quantitative information about their q-dependence. In Fig. 2(a), we introduce our fitting model based on ten Gaussian profiles, and we assign one peak to the elastic line at 0 meV (dashed line), three peaks to a known phonon and multiphonon contributions (solid lines) from Refs. [45–47] (see also Sec. IV in the Supplemental Material [40]), and additional six peaks

(area-filled profiles) to all the other excitations extending up to approximately 500 meV. For the details of our fitting analysis and the implemented constraints, refer to Sec. V of the Supplemental Material [40]. In Fig. 2(c), we report a summary of the fitted energies for the six area-filled peaks. Except for the lowest-energy excitation behaving as an acoustic mode, all the other excitations are optical modes: Interestingly, their *q*-averaged energies appear to follow a harmonic sequence with respect to the first optical mode at E_0, i.e., E_0 ($\sim 97 \pm 1$ meV), $2E_0$ ($\sim 188 \pm 4$ meV), $3E_0$ ($\sim 286 \pm 15$ meV), $4E_0$ ($\sim 376 \pm 17$ meV), and $5E_0$ ($\sim 478 \pm 19$ meV).

From inelastic-neutron-scattering studies [37,38], the single magnon ($\Delta S_z = 1$ excitation) in α-Fe$_2$O$_3$ single crystal is known to exhibit both an acoustic and an optical branch. In Figs. 2(b) and 2(c), we overlay to the RIXS data the single-magnon dispersion calculated following Ref. [38]. A remarkable consistency exists between the calculated dispersion of the $\Delta S_z = 1$ branches and the excitations probed by RIXS below 100 meV. On one hand, this important observation reveals the magnetic nature of the first two excitations in Fig. 2(c). On the other hand, this result shows that the out-of-plane single magnon has the same energy either in the bulk or in the thin films (30 and 15 nm thick). This suggests that the single magnon in hematite is not subject to thickness-related phenomena or to electronic band reconstruction acting on the confinement direction [14,15]. Finally, we propose that the observed harmonic sequence of optical modes at $2E_0$, $3E_0$, $4E_0$, and

$5E_0$ energies may share the same magnetic origin as the fundamental mode $\Delta S_z = 1$ at E_0 energy.

IV. CALCULATIONS AND DISCUSSION

To assess the nature of the low-energy harmoniclike sequence of excitations, we use the LDA + DMFT AIM, a recently introduced method to simulate the RIXS spectra of correlated transition-metal oxides [31,48–50]. The LDA + DMFT calculations are performed for the valence electrons (Fe 3*d* and O 2*p* orbitals are included) in the experimental crystal structure [51–54]. In addition to the *ab initio* band structure, three parameters are required: Hubbard U, Hund's coupling J, and charge-transfer energy Δ_{CT} [31,49,53,55]. These are determined to be $U = 6.5$ eV, $\Delta_{\text{CT}} = 2.4$ eV, and $J = 1.0$ eV by matching the experimental RIXS high-energy excitations (above 1 eV) with LDA + DMFT AIM calculations, as detailed in the Sec. VI of the Supplemental Material [40].

Figure 3(a) shows the computed RIXS intensities evaluated using the Kramers-Heisenberg formula (see Sec. VI of the Supplemental Material [40]), which implements the dipole transitions for the photon absorption and emission. The spectrum (black line) exhibits an intense peak at $E_{\text{SF}} = 66$ meV, followed by four equally spaced peaks at $2E_{\text{SF}}$, $3E_{\text{SF}}$, $4E_{\text{SF}}$, and $5E_{\text{SF}}$ with decreasing intensities, similar to the experimental observation represented by the fitted Gaussian components [color-filled areas in Fig. 3(a)]. Analyzing the ground-state and final-state wave functions
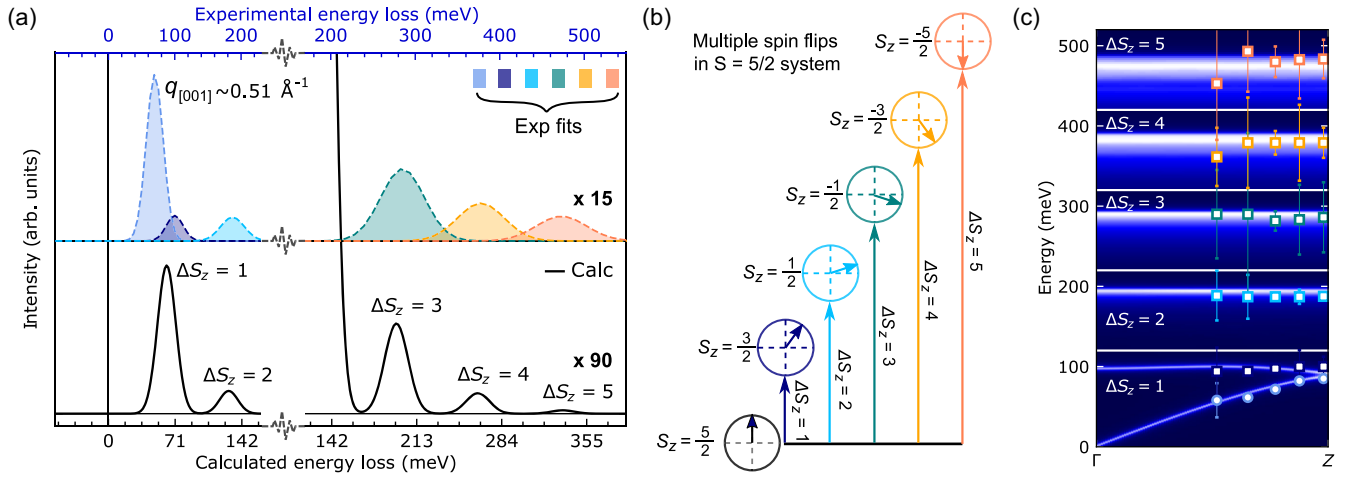

FIG. 3. Calculations of magnetic excitations for α-Fe$_2$O$_3$. (a) Calculated RIXS spectrum of multispin-flip excitations using the LDA + DMFT AIM (black solid line). The color-filled Gaussians are the fitting results of the experimental RIXS data in Fig. 2(a). The elastic peak is removed in both spectra. The calculated spectral weight for $\Delta S_z = 3$, 4, 5 underestimates the measured intensity, and possible arguments are presented in Sec. VI of Ref. [40]. (b) A diagram of the possible multispin-flip excitations for an $S = \frac{5}{2}$ system using a local picture. (c) The *q*-resolved DOS of the AFM magnons. The single-magnon is calculated within the Heisenberg model. The multimagnons are obtained as a convolution of multiple single magnons, as explained in the text. For each ΔS_z mode, the DOS is normalized to the maximum achieved in the investigated *q* range. The horizontal white lines define the energy windows used for each DOS normalization. The markers are the experimental RIXS energies identified in Fig. 2(c) for the acoustic (circles) and optical (squares) branches.

(see the Table III in the Supplemental Material [40]), we identify the calculated peaks as $\Delta S_z = 1, 2, 3, 4,$ and 5 multispin-flip excitations with increasing energy; see the diagram in Fig. 3(b). Although there is no analogy of the acoustic magnon branch in AIM, the local spin-flip excitations captured by the Anderson impurity model coincide with the real energy of the flat optical magnon branch in a 3D antiferromagnet.

The LDA + DMFT AIM, however, appears to underestimate the peak positions of $\Delta S_z = 1, 2, 3, 4,$ and 5 excitations by a factor of approximately 1.4 with respect to the experiment; see the different scales used for the bottom (calculation) and top (experiment) axes in Fig. 3(a). This result reflects an underestimation of the effective interatomic spin exchange by the present LDA + DMFT model. A more accurate description of the effective exchange parameters may require inclusion of interaction on the oxygen sites [56], which is beyond the scope of this work. Furthermore, we note that the calculation underestimates the spectral weight of $\Delta S_z = 3, 4, 5$ excitations by a factor of approximately 4 relative to that of $\Delta S_z = 1, 2$ excitations. Possible causes for this are discussed in Sec. VI of Ref. [40].

To address the absolute energy and $\boldsymbol{q}$-dispersion of these excitations, we resort to the Heisenberg model $H = \sum_{i,j} J_{ij} \mathbf{S}_i \cdot \mathbf{S}_j$ with the exchange parameters of bulk α-Fe$_2$O$_3$ [37,38]. We derive first the dispersion $\varepsilon(\boldsymbol{q})$ of the single-magnon acoustic and optical branches, being the two eigenmodes of H for α-Fe$_2$O$_3$. For the higher-order spin-flip excitations ($\Delta S_z \geq 2$), we represent them as multiple, noninteracting magnons rather than bound states of several magnons. Therefore, a multimagnon excitation at a momentum $\boldsymbol{q}$ is expressed as a product (convolution) of the single magnons with momenta $(\boldsymbol{q}_1, \boldsymbol{q}_2, \ldots)$ constrained by the momentum conservation, i.e., $\boldsymbol{q} = \boldsymbol{q}_1 + \boldsymbol{q}_2 + \ldots$. Evaluating the n-particle Green's functions $G_n(\omega, \boldsymbol{q}) = [\omega - \varepsilon(\boldsymbol{q}_1) - \varepsilon(\boldsymbol{q}_2) - \cdots - \varepsilon(\boldsymbol{q}_n)]^{-1}$ for single magnons across the whole Brillouin zone eventually produces the spectral density in energy-momentum space for the $\Delta S_z = n$ excitation.

In Fig. 3(c), we display the resulting density of states (DOS) for $\Delta S_z = 1, 2, 3, 4,$ and 5 multimagnon excitations. The $\Delta S_z = 1$ acoustic and optical branches topping around 98 meV reproduce the experimental RIXS results (circle and square symbols overlaid to the DOS). Although the calculated multimagnon spectra present a broad continuum, the spectral weights actually accumulate in narrow peaks at multiples of approximately 98 meV. This reflects the flat nature of the optical magnon branch in a 3D antiferromagnet, contrary to a 1D system [36], and well captures the experimental RIXS results reproduced in Fig. 3(c). Thanks to this agreement, we fully corroborate the assignment of the measured harmoniclike peaks as $\Delta S_z = 1, 2, 3, 4,$ and 5 magnetic excitations, and infer their character as multiple noninteracting magnons. The noninteracting behavior is an important aspect for the magnon propagation in α-Fe$_2$O$_3$, directly relevant for spintronics and consistent with the recently reported long-magnon-propagation length [5]. We further note that the total multimagnon contribution observed in α-Fe$_2$O$_3$ amounts up to 10% of the single-magnon spectral weight (including the effect of the RIXS cross section).

V. MULTIMAGNON EXCITATIONS IN RIXS

Ultimately, our observations raise the question of the origin of multimagnon excitations in the RIXS spectra, in light of the dipolar character of the photon emission and absorption processes exchanging at most two quanta of angular momentum. To answer this, we investigate the spin character of the RIXS intermediate states $|m\rangle$. To simplify the analysis, we employ an atomic model [30,57], which has the same symmetry properties as AIM but allows explicit evaluation of the intermediate states $|m\rangle$ (see Sec. VII of the Supplemental Material [40] for details). We then examine the amplitudes $I_m = |\langle f|T_e|m\rangle\langle m|T_i|g\rangle|^2$ [see Eq. (S1) in the Supplemental Material [40]] for the transition from the ground state $|g\rangle$ to the final state $|f\rangle$ via $|m\rangle$ [58]. Note that the amplitudes I_m are only indicative of whether a given channel is available or not. They shall not be summed up to estimate the total RIXS amplitude, which arises due to interference of all the different channels.

Since the electric dipole transitions conserve the electron spin, the spin-flip excitations are enabled by spin-nonconserving terms in the system Hamiltonian. It is therefore crucial to understand which are the active symmetry-breaking terms and how they affect the final states in RIXS. The initial state $|g\rangle$ and final states $|f\rangle$ of the studied RIXS process are orbital singlets, $S = \frac{5}{2}$ eigenstates of the spin S_{3d}, thanks to their half-filled $3d^5$ character and the strong Hund's coupling dominating over the crystal field (CF). These states ($|g\rangle$ and $|f\rangle$) remain approximately so even if the weak $3d$ spin-orbit coupling SOC$_{3d}$ is considered. The completely filled $2p$ core shell, instead, is subject to the strong spin-orbit-coupling SOC$_{2p}$ but negligible CF; thus, it can be labeled by the total angular momentum J_{2p}. In the intermediate state $|i\rangle$, when a $2p$ electron is promoted to the $3d$ state, the core-valence interaction CV$_{2p\leftrightarrow 3d}$ [59] becomes relevant as it entangles the partially filled $2p$ and $3d$ states due to its multipole terms. As a result, CV$_{2p\leftrightarrow 3d}$ conserves only the total angular momentum of both shells $J_{2p} + J_{3d}$, but not the J_{2p} and J_{3d} angular momenta separately. A summary of the conserved quantities for each active interaction is presented in Table I.

On the basis of this information, we disentangle the role of the different terms, i.e., SOC$_{2p}$, SOC$_{3d}$, CV$_{2p\leftrightarrow 3d}$, and CF, in the atomic model and uncover their contribution to I_m by switching them on and off independently.

TABLE I. Conserved quantities for the $2p$ and $3d$ shells (columns) under SOC_{2p}, SOC_{3d}, $CV_{2p\leftrightarrow3d}$, and CF interactions (rows). The ✓ marker indicates that the corresponding operators commute, while the × marker indicates noncommuting operators. An observable is conserved if its column contains only ✓ markers; i.e., the interactions with the × mark are not included in the Hamiltonian. The red color highlights the broken quantities that are critical for accessing multispin excitations enabling the transfer of angular momentum to the electron spin. The green color highlights the broken quantity that expands the available angular momentum beyond $\Delta J_z = 2$ exchanged by the absorbed and emitted photons.

No.	$J_{2p} + J_{3d}$	J_{2p}	J_{3d}	L_{3d}	$S_{2p} + S_{3d}$	S_{2p}	S_{3d}
SOC_{2p}	✓	✓	✓	✓	×	×	✓
SOC_{3d}	✓	✓	✓	×	×	✓	×
$CV_{2p\leftrightarrow3d}$	✓	×	×	×	✓	×	×
CF	×	✓	×	×	✓	✓	✓

Considering the photon-electron interaction under dipole approximation, the following selection rule applies to the photon absorption or emission process, e.g., $\Delta J_z = 0, \pm 1$ [17]. As we focus here on spin excitations, we need to transfer the available angular momentum to the spin of the electrons by activating proper spin-orbital-coupling channels.

With all interactions on [see Fig. 4(a)], a large number of nondegenerate $|m\rangle$ states is accessible, and their amplitude is finite for $\Delta S_z = 1, 2, 3, 4,$ and 5. With reference to Table I, when these four interactions are simultaneously active, no quantity is conserved (a quantity is conserved when it is so for each active interaction). In particular, S_{3d} is not a good quantum number for the intermediate states $|m\rangle$. This is reflected by $\langle \hat{S}_{3d,z} \rangle$ and $\sqrt{\langle \hat{\mathbf{S}}_{3d}^2 \rangle}$ differing from the integer n and $\sqrt{n(n+1)}$, respectively; see inset of Fig. 4(a).

In Fig. 4(b), we switch off the two terms that break S_{3d}, respectively, $CV_{2p\leftrightarrow3d}$ and SOC_{3d} (see Table I). In this case, S_{3d} is conserved, as demonstrated by the integer value of, e.g., $\langle \hat{S}_{3d,z} \rangle$. A finite I_m is obtained only for $\Delta S_z = 1$ due to the spin mixing in the $2p$ state by SOC_{2p} [14,16,26]; i.e., electrons with opposite spin can be excited or deexcited in the photon absorption or emission process.

Comparing the two scenarios in Figs. 4(a) and 4(b), it clearly emerges the key role of $CV_{2p\leftrightarrow3d}$ and SOC_{3d} in allowing multispin excitations in the RIXS process. The nonconservation of S_{3d} caused by the spin-orbital mix in the Fe $3d$ states enables the transfer of the angular momentum to the electron spin. This can happen directly by SOC_{3d} or indirectly due to the combination of SOC_{2p} and the multipole part of $CV_{2p\leftrightarrow3d}$. In both cases, a number of states $|m\rangle$ have overlap with initial and final states of different S_z, leading to multispin-flip excitations.
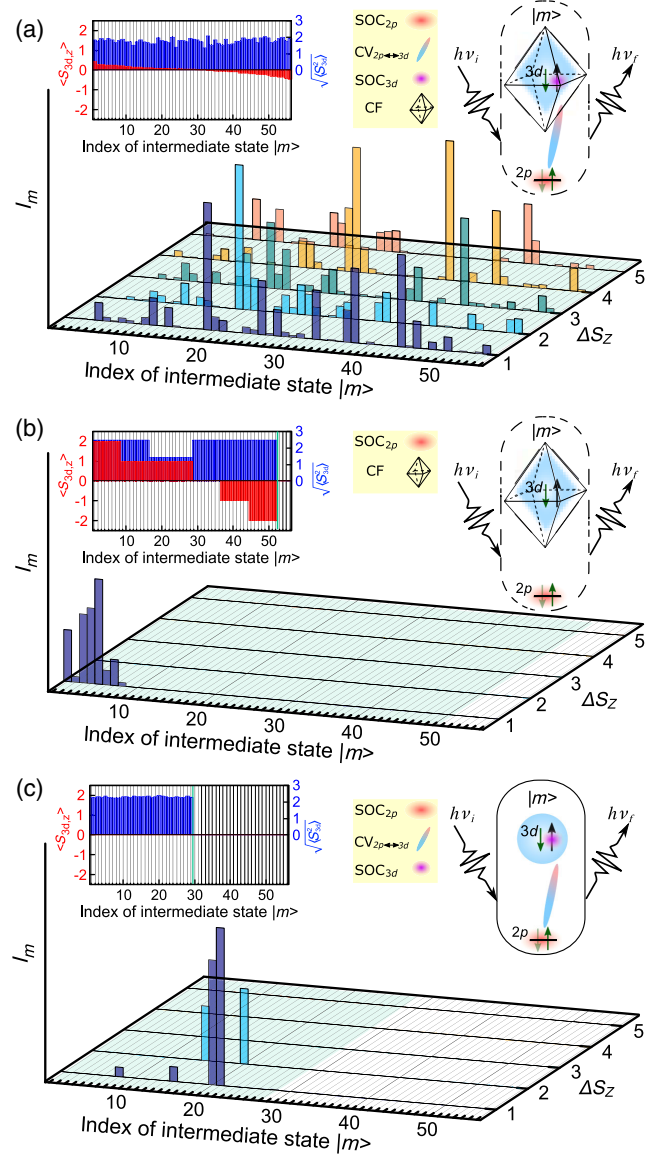

FIG. 4. Calculated RIXS amplitude $I_m = |\langle f|T_e|m\rangle\langle m|T_i|g\rangle|^2$ of the magnetic excitations [the numerator part of the first term in the Kramers-Heisenberg formula; see Eq. (S1) of the Supplemental Material [40]] from the ground state $|g\rangle$ to the final state $|f\rangle$ via different intermediate states $|m\rangle$ with energies $E_m \in [E_{L_3} \pm 0.3 \text{ eV}]$ (E_{L_3} denotes the Fe-e_g absorption energy), using the local atomic model. (a) Amplitude I_m when SOC_{3d}, SOC_{2p}, $CV_{2p\leftrightarrow3d}$, and CF interactions are switched on. (b) Amplitude I_m when SOC_{3d} and $CV_{2p\leftrightarrow3d}$ are off (i.e., SOC_{2p} and CF are on). (c) Amplitude I_m when CF is off (i.e., SOC_{3d}, SOC_{2p}, $CV_{2p\leftrightarrow3d}$ are on). Within the selected L_3-edge energy window, we consider 56, 51, and 29 $|m\rangle$ states with different eigenenergies E_m (indicated by the green shaded area), respectively, for (a), (b), and (c), accounting for 95% of the total calculated RIXS intensity (integrated over the energy loss) at a given photon energy (E_{L_3}). The insets on the left of each plot summarize the $\langle \hat{S}_{3d,z} \rangle$ and $\sqrt{\langle \hat{\mathbf{S}}_{3d}^2 \rangle}$ values on the Fe $3d$ shell in these intermediate states.

Finally, we discuss the role of CF. In Fig. 4(c), we keep all interactions on but we switch off the CF, i.e., in condition of spherical symmetry. The total angular momentum $J_{3d} + J_{2p}$ is conserved, but not S_{3d}. A finite I_m is found for multispin excitations, but only up to $\Delta S_z = 2$. In this case, in fact, only the angular momentum carried by the absorbed and emitted photons is the source of ΔS_z, which is therefore less than or equal to 2. On the contrary, when the spherical symmetry is broken, i.e., CF $\neq 0$ as in Fig. 4(a), the $J_{3d} + J_{2p}$ quantity is not conserved, and the crystal lattice acts as a reservoir of angular momentum, allowing the exchange of more than two quanta of ΔJ_z. Multispin excitations beyond $\Delta S_z = 2$ [22,33] then become possible, reaching $\Delta S_z = 2S$ in a spin-S system, e.g., $\Delta S_z = 5$ for α-Fe_2O_3. Following this logic, we predict to resolve multispin excitations up to $\Delta S_z = 3$ for CoO, an $S = \frac{3}{2}$ system. For a quantitative comparison of the individual strength of $CV_{2p \leftrightarrow 3d}$, SOC_{3d}, SOC_{2p} onto the multispin-flip RIXS intensity, we refer to Fig. S7 in the Supplemental Material [40].

VI. CONCLUSION

In conclusion, we unveil magnons and their q-dynamics in $S = \frac{5}{2}$ α-Fe_2O_3 thin films by combining RIXS measurements and calculations based on LDA + DMFT AIM and the Heisenberg model. Below 100 meV, we observe the single-magnon mode with equivalent energy in 15- and 30-nm films. This mode displays a q-dispersion matching the one of the bulk, thus indicating the robustness of out-of-plane magnons in hematite down to 15 nm. Furthermore, an unexpected sequence of equally spaced excitations is observed in the (100–500)-meV range assigned to $\Delta S_z = 1, 2, 3, 4$, and 5 spin-flip transitions corresponding to multiple noninteracting magnons. Based on these results, we convey a comprehensive description of the energy, character, and momentum dependence of magnons in hematite thin films, with potential impact on magnon transport (e.g., hematite offers noninteracting, long-range traveling magnons with finite contribution from multimagnon modes) and on magnon pumping (e.g., pump frequency should be set away from the multimagnon energies to minimize dissipation channels). At the same time, our study generalizes the use of L-edge RIXS as a multispin-excitation probe being able to access magnetic excitations up to $\Delta S_z = 2S$. We demonstrate that the breaking of S_{3d}, and the consequent spin-orbital mix in the valence shell, is the key element for opening the path to multispin-flip excitations. Furthermore, for $\Delta S_z > 2$, we introduce the key role of the lattice-breaking spherical symmetry acting as a reservoir of angular momentum and complementing the one carried by the absorbed and emitted photons. Such a mechanism can generate interesting consequences. For example, in multiorbital systems (under proper conditions of, e.g., resonant edge,

crystal-field symmetry, Hund's coupling), we could control the intensity of the spin and multispin-flip excitations by manipulating the local crystal environment through external perturbations, like, e.g., strain, light pulses, gating, and chemical pressure. This opportunity could represent a novel route to tune magnetic excitations in spintronic materials, deserving further studies. Ultimately, our method proves the feasibility of magnon studies in devicelike conditions, i.e., thin films, encouraging future investigations under, e.g., electric gating or photoexcitation.

As a final note, we underline that understanding multimagnons beyond $\Delta S_z > 2$ by means of a two-photon-scattering process is a very timely and active topic stimulated by the recently improved RIXS spectrometers. Indeed, similar conclusions on the key role of the CF in the context of multimagnons with $\Delta S_z > 2$ have also been reported by Elnaggar *et al.* while studying the azimuthal dependence of α-Fe_2O_3 single crystals [60].

[1] T. Jungwirth, X. Marti, P. Wadley, and J. Wunderlich, *Antiferromagnetic Spintronics*, Nat. Nanotechnol. **11**, 231 (2016).

[2] V. Baltz, A. Manchon, M. Tsoi, T. Moriyama, T. Ono, and Y. Tserkovnyak, *Antiferromagnetic Spintronics*, Rev. Mod. Phys. **90**, 015005 (2018).

[3] H. Wang, C. Du, P. C. Hammel, and F. Yang, *Antiferromagnonic Spin Transport from* $Y_3Fe_5O_{12}$ *into* NiO, Phys. Rev. Lett. **113**, 097202 (2014).

[4] S. M. Wu, W. Zhang, A. KC, P. Borisov, J. E. Pearson, J. S. Jiang, D. Lederman, A. Hoffmann, and A. Bhattacharya, *Antiferromagnetic Spin Seebeck Effect*, Phys. Rev. Lett. **116**, 097204 (2016).

[5] R. Lebrun, A. Ross, S. Bender, A. Qaiumzadeh, L. Baldrati, J. Cramer, A. Brataas, R. Duine, and M. Kläui, *Tunable Long-Distance Spin Transport in a Crystalline Antiferromagnetic Iron Oxide*, Nature (London) **561**, 222 (2018).

[6] R. Lebrun, A. Ross, O. Gomonay, V. Baltz, U. Ebels, A.-L. Barra, A. Qaiumzadeh, A. Brataas, J. Sinova, and M. Kläui, *Long-Distance Spin-Transport across the Morin Phase Transition up to Room Temperature in Ultra-Low Damping*

Single Crystals of the Antiferromagnet α-Fe$_2$O$_3$, Nat. Commun. **11**, 6332 (2020).

[7] J. Han, P. Zhang, Z. Bi, Y. Fan, T. S. Safi, J. Xiang, J. Finley, L. Fu, R. Cheng, and L. Liu, *Birefringence-like Spin Transport via Linearly Polarized Antiferromagnetic Magnons*, Nat. Nanotechnol. **15**, 563 (2020).

[8] Y. Cheng, S. Yu, A. S. Ahmed, M. Zhu, Y. Rao, M. Ghazisaeidi, J. Hwang, and F. Yang, *Anisotropic Magneto-resistance and Nontrivial Spin Hall Magnetoresistance in* Pt/α-Fe$_2$O$_3$ *Bilayers*, Phys. Rev. B **100**, 220408(R) (2019).

[9] P. Zhang, J. Finley, T. Safi, and L. Liu, *Quantitative Study on Current-Induced Effect in an Antiferromagnet Insulator/* Pt *Bilayer Film*, Phys. Rev. Lett. **123**, 247206 (2019).

[10] Y. Cheng, S. Yu, M. Zhu, J. Hwang, and F. Yang, *Electrical Switching of Tristate Antiferromagnetic Néel Order in* α-Fe$_2$O$_3$ *Epitaxial Films*, Phys. Rev. Lett. **124**, 027202 (2020).

[11] E. Cogulu, N. N. Statuto, Y. Cheng, F. Yang, R. V. Chopdekar, H. Ohldag, and A. D. Kent, *Direct Imaging of Electrical Switching of Antiferromagnetic Néel Order in* α-Fe$_2$O$_3$ *Epitaxial Films*, Phys. Rev. B **103**, L100405 (2021).

[12] D. Meyers *et al.*, *Magnetism in Iridate Heterostructures Leveraged by Structural Distortions*, Sci. Rep. **9**, 4263 (2019).

[13] O. Ivashko, M. Horio, W. Wan, N. B. Christensen, D. E. McNally, E. Paris, Y. Tseng, N. E. Shaik, H. M. Rønnow, H. I. Wei, C. Adamo, C. Lichtensteiger, M. Gibert, M. R. Beasley, K. M. Shen, J. M. Tomczak, T. Schmitt, and J. Chang, *Strain-Engineering Mott-Insulating* La$_2$CuO$_4$, Nat. Commun. **10**, 786 (2019).

[14] J. Pelliciari, S. Lee, K. Gilmore, J. Li, Y. Gu, A. Barbour, I. Jarrige, C. H. Ahn, F. J. Walker, and V. Bisogni, *Tuning Spin Excitations in Magnetic Films by Confinement*, Nat. Mater. **20**, 188 (2021).

[15] J. Pelliciari, S. Karakuzu, Q. Song, R. Arpaia, A. Nag, M. Rossi, J. Li, T. Yu, X. Chen, R. Peng, M. García-Fernández, A. C. Walters, Q. Wang, J. Zhao, G. Ghiringhelli, D. Feng, T. A. Maier, K.-J. Zhou, S. Johnston, and R. Comin, *Evolution of Spin Excitations from Bulk to Monolayer* FeSe, Nat. Commun. **12**, 3122 (2021).

[16] L. Braicovich, J. van den Brink, V. Bisogni, M. M. Sala, L. J. P. Ament, N. B. Brookes, G. M. De Luca, M. Salluzzo, T. Schmitt, V. N. Strocov, and G. Ghiringhelli, *Magnetic Excitations and Phase Separation in the Underdoped* La$_{2-x}$Sr$_x$CuO$_4$ *Superconductor Measured by Resonant Inelastic X-Ray Scattering*, Phys. Rev. Lett. **104**, 077002 (2010).

[17] L. J. P. Ament, M. van Veenendaal, T. P. Devereaux, J. P. Hill, and J. van den Brink, *Resonant Inelastic X-Ray Scattering Studies of Elementary Excitations*, Rev. Mod. Phys. **83**, 705 (2011).

[18] G. Fabbris, D. Meyers, L. Xu, V. M. Katukuri, L. Hozoi, X. Liu, Z.-Y. Chen, J. Okamoto, T. Schmitt, A. Uldry, B. Delley, G. D. Gu, D. Prabhakaran, A. T. Boothroyd, J. van den Brink, D. J. Huang, and M. P. M. Dean, *Doping Dependence of Collective Spin and Orbital Excitations in the Spin-1 Quantum Antiferromagnet* La$_{2-x}$Sr$_x$NiO$_4$ *Observed by X Rays*, Phys. Rev. Lett. **118**, 156402 (2017).

[19] D. Betto, Y. Y. Peng, S. B. Porter, G. Berti, A. Calloni, G. Ghiringhelli, and N. B. Brookes, *Three-Dimensional*

Dispersion of Spin Waves Measured in NiO *by Resonant Inelastic X-Ray Scattering*, Phys. Rev. B **96**, 020409(R) (2017).

[20] H. Elnaggar, R.-P. Wang, S. Lafuerza, E. Paris, Y. Tseng, D. McNally, A. Komarek, M. Haverkort, M. Sikora, T. Schmitt, and F. M. F. de Groot, *Magnetic Contrast at Spin-Flip Excitations: An Advanced X-Ray Spectroscopy Tool to Study Magnetic-Ordering*, ACS Appl. Mater. Interfaces **11**, 36213 (2019).

[21] J. Li, L. Xu, M. Garcia-Fernandez, A. Nag, H. C. Robarts, A. C. Walters, X. Liu, J. Zhou, K. Wohlfeld, J. van den Brink, H. Ding, and K.-J. Zhou, *Unraveling the Orbital Physics in a Canonical Orbital System* KCuF$_3$, Phys. Rev. Lett. **126**, 106401 (2021).

[22] A. Nag, H. C. Robarts, F. Wenzel, J. Li, H. Elnaggar, R.-P. Wang, A. C. Walters, M. García-Fernández, F. M. F. de Groot, M. W. Haverkort, and K.-J. Zhou, *Many-Body Physics of Single and Double Spin-Flip Excitations in* NiO, Phys. Rev. Lett. **124**, 067202 (2020).

[23] D. Betto, R. Fumagalli, L. Martinelli, M. Rossi, R. Piombo, K. Yoshimi, D. Di Castro, E. Di Gennaro, A. Sambri, D. Bonn, G. A. Sawatzky, L. Braicovich, N. B. Brookes, J. Lorenzana, and G. Ghiringhelli, *Multiple-Magnon Excitations Shape the Spin Spectrum of Cuprate Parent Compounds*, Phys. Rev. B **103**, L140409 (2021).

[24] L. Martinelli, D. Betto, K. Kummer, R. Arpaia, L. Braicovich, D. Di Castro, N. B. Brookes, M. Moretti Sala, and G. Ghiringhelli, *Fractional Spin Excitations in the Infinite-Layer Cuprate* CaCuO$_2$, Phys. Rev. X **12**, 021041 (2022).

[25] Y. Gu, Y. Wang, J. Lin, J. Pelliciari, J. Li, M.-G. Han, M. Schmidt, G. Kotliar, C. Mazzoli, M. P. M. Dean, and V. Bisogni, *Site-Specific Electronic and Magnetic Excitations of the Skyrmion Material* Cu$_2$OSeO$_3$, Commun. Phys. **5**, 156 (2022).

[26] M. P. M. Dean, R. S. Springell, C. Monney, K. J. Zhou, J. Pereiro, I. Božović, B. Dalla Piazza, H. M. Rønnow, E. Morenzoni, J. van den Brink, T. Schmitt, and J. P. Hill, *Spin Excitations in a Single* La$_2$CuO$_4$ *Layer*, Nat. Mater. **11**, 850 (2012).

[27] N. B. Brookes, D. Betto, K. Cao, Y. Lu, K. Kummer, and F. Giustino, *Spin Waves in Metallic Iron and Nickel Measured by Soft X-Ray Resonant Inelastic Scattering*, Phys. Rev. B **102**, 064412 (2020).

[28] M. W. Haverkort, *Theory of Resonant Inelastic X-Ray Scattering by Collective Magnetic Excitations*, Phys. Rev. Lett. **105**, 167404 (2010).

[29] P. Zimmermann, R. J. Green, M. W. Haverkort, and F. M. F. de Groot, QUANTY4RIXS: *A Program for Crystal Field Multiplet Calculations of RIXS and RIXS-MCD Spectra Using* QUANTY, J. Synchrotron Radiat. **25**, 899 (2018).

[30] Y. Wang, G. Fabbris, M. Dean, and G. Kotliar, *Edrixs: An Open Source Toolkit for Simulating Spectra of Resonant Inelastic X-Ray Scattering*, Comput. Phys. Commun. **243**, 151 (2019).

[31] A. Hariki, M. Winder, T. Uozumi, and J. Kuneš, LDA + DMFT *Approach to Resonant Inelastic X-Ray Scattering in Correlated Materials*, Phys. Rev. B **101**, 115130 (2020).

[32] K. Gilmore, J. Pelliciari, Y. Huang, J. J. Kas, M. Dantz, V. N. Strocov, S. Kasahara, Y. Matsuda, T. Das, T. Shibauchi, and T. Schmitt, *Description of Resonant*

Inelastic X-Ray Scattering in Correlated Metals, Phys. Rev. X **11**, 031013 (2021).

[33] G. Ghiringhelli, A. Piazzalunga, C. Dallera, T. Schmitt, V. N. Strocov, J. Schlappa, L. Patthey, X. Wang, H. Berger, and M. Grioni, *Observation of Two Nondispersive Magnetic Excitations in NiO by Resonant Inelastic Soft-X-Ray Scattering*, Phys. Rev. Lett. **102**, 027401 (2009).

[34] V. Bisogni, S. Kourtis, C. Monney, K. Zhou, R. Kraus, C. Sekar, V. Strocov, B. Büchner, J. van den Brink, L. Braicovich, T. Schmitt, M. Daghofer, and J. Geck, *Femtosecond Dynamics of Momentum-Dependent Magnetic Excitations from Resonant Inelastic X-Ray Scattering in $CaCu_2O_3$*, Phys. Rev. Lett. **112**, 147401 (2014).

[35] J. Schlappa, U. Kumar, K. J. Zhou, S. Singh, M. Mourigal, V. N. Strocov, A. Revcolevschi, L. Patthey, H. M. Rønnow, S. Johnston, and T. Schmitt, *Probing Multi-Spinon Excitations outside of the Two-Spinon Continuum in the Antiferromagnetic Spin Chain Cuprate Sr_2CuO_3*, Nat. Commun. **9**, 5394 (2018).

[36] A. Nag, A. Nocera, S. Agrestini, M. Garcia-Fernandez, A. C. Walters, S.-W. Cheong, S. Johnston, and K.-J. Zhou, *Quadrupolar Magnetic Excitations in an Isotropic Spin-1 Antiferromagnet*, Nat. Commun. **13**, 2327 (2022).

[37] E. Samuelsen, *Spin Waves in Antiferromagnets with Corundum Structure*, Physica (Amsterdam) **43**, 353 (1969).

[38] E. J. Samuelsen and G. Shirane, *Inelastic Neutron Scattering Investigation of Spin Waves and Magnetic Interactions in α-Fe_2O_3*, Phys. Status Solidi (b) **42**, 241 (1970).

[39] C. G. Shull, W. A. Strauser, and E. O. Wollan, *Neutron Diffraction by Paramagnetic and Antiferromagnetic Substances*, Phys. Rev. **83**, 333 (1951).

[40] See Supplemental Material at http://link.aps.org/supplemental/10.1103/PhysRevX.13.011012 for details about samples, experimental data fitting, and theoretical calculation.

[41] J. Dvorak, I. Jarrige, V. Bisogni, S. Coburn, and W. Leonhardt, *Towards 10 meV Resolution: The Design of an Ultrahigh Resolution Soft X-Ray RIXS Spectrometer*, Rev. Sci. Instrum. **87**, 115109 (2016).

[42] P. Kuiper, B. G. Searle, P. Rudolf, L. H. Tjeng, and C. T. Chen, *X-Ray Magnetic Dichroism of Antiferromagnet Fe_2O_3: The Orientation of Magnetic Moments Observed by Fe $2p$ X-Ray Absorption Spectroscopy*, Phys. Rev. Lett. **70**, 1549 (1993).

[43] J. Miyawaki, S. Suga, H. Fujiwara, M. Urasaki, H. Ikeno, H. Niwa, H. Kiuchi, and Y. Harada, *Dzyaloshinskii-Moriya Interaction in α-Fe_2O_3 Measured by Magnetic Circular Dichroism in Resonant Inelastic Soft X-Ray Scattering*, Phys. Rev. B **96**, 214420 (2017).

[44] D. S. Ellis, R.-P. Wang, D. Wong, J. K. Cooper, C. Schulz, Y.-D. Chuang, Y. Piekner, D. A. Grave, M. Schleuning, D. Friedrich, F. M. F. de Groot, and A. Rothschild, *Electronic Excitations of α-Fe_2O_3 Heteroepitaxial Films Measured by Resonant Inelastic X-Ray Scattering at the Fe L Edge*, Phys. Rev. B **105**, 075101 (2022).

[45] M. J. Massey, U. Baier, R. Merlin, and W. H. Weber, *Effects of Pressure and Isotopic Substitution on the Raman Spectrum of α-Fe_2O_3: Identification of Two-Magnon Scattering*, Phys. Rev. B **41**, 7822 (1990).

[46] S. Azuma, M. Sato, Y. Fujimaki, S. Uchida, Y. Tanabe, and E. Hanamura, *Optical Response Due to Many Magnons in α-Fe_2O_3*, Phys. Rev. B **71**, 014429 (2005).

[47] I. Chamritski and G. Burns, *Infrared- and Raman-Active Phonons of Magnetite, Maghemite, and Hematite: A Computer Simulation and Spectroscopic Study*, J. Phys. Chem. B **109**, 4965 (2005).

[48] A. Hariki, M. Winder, and J. Kuneš, *Continuum Charge Excitations in High-Valence Transition-Metal Oxides Revealed by Resonant Inelastic X-Ray Scattering*, Phys. Rev. Lett. **121**, 126403 (2018).

[49] M. Winder, A. Hariki, and J. Kuneš, *X-Ray Spectroscopy of the Rare-Earth Nickelate $LuNiO_3$: LDA + DMFT Study*, Phys. Rev. B **102**, 085155 (2020).

[50] K. Higashi, M. Winder, J. Kuneš, and A. Hariki, *Core-Level X-Ray Spectroscopy of Infinite-Layer Nickelate: LDA + DMFT Study*, Phys. Rev. X **11**, 041009 (2021).

[51] A. Georges, G. Kotliar, W. Krauth, and M. J. Rozenberg, *Dynamical Mean-Field Theory of Strongly Correlated Fermion Systems and the Limit of Infinite Dimensions*, Rev. Mod. Phys. **68**, 13 (1996).

[52] G. Kotliar, S. Y. Savrasov, K. Haule, V. S. Oudovenko, O. Parcollet, and C. A. Marianetti, *Electronic Structure Calculations with Dynamical Mean-Field Theory*, Rev. Mod. Phys. **78**, 865 (2006).

[53] J. Kuneš, D. M. Korotin, M. A. Korotin, V. I. Anisimov, and P. Werner, *Pressure-Driven Metal-Insulator Transition in Hematite from Dynamical Mean-Field Theory*, Phys. Rev. Lett. **102**, 146402 (2009).

[54] J. Kuneš, I. Leonov, M. Kollar, K. Byczuk, V. I. Anisimov, and D. Vollhardt, *Dynamical Mean-Field Approach to Materials with Strong Electronic Correlations*, Eur. Phys. J. Special Topics **180**, 5 (2009).

[55] In the LDA + DMFT self-consistent calculations, the double-counting correction value μ_{DC} is adjusted as a parameter. The charge-transfer energy Δ_{CT} is defined as $\Delta_{CT} = \varepsilon_d - \mu_{DC} + 5 \times U_{av} - \varepsilon_p$, where ε_d (ε_p) is the on-site energy of Fe $3d$ (O $2p$) states in the LDA result, and U_{av} is the averaged Coulomb interaction on the Fe $3d$ shell [49,50].

[56] R. Logemann, A. N. Rudenko, M. I. Katsnelson, and A. Kirilyuk, *Exchange Interactions in Transition Metal Oxides: The Role of Oxygen Spin Polarization*, J. Phys. Condens. Matter **29**, 335801 (2017).

[57] F. M. de Groot *et al.*, *$2p$ X-Ray Absorption Spectroscopy of $3d$ Transition Metal Systems*, J. Electron Spectrosc. Relat. Phenom. **249**, 147061 (2021).

[58] Note that in the LDA + DMFT AIM calculation, a resolvent technique is used for computing the RIXS intensities, and thus, such $|m\rangle$-resolved amplitudes (I_m) are not available [31,40].

[59] M. Ghiasi, A. Hariki, M. Winder, J. Kuneš, A. Regoutz, T.-L. Lee, Y. Hu, J.-P. Rueff, and F. M. F. de Groot, *Charge-Transfer Effect in Hard X-Ray $1s$ and $2p$ Photoemission Spectra: LDA + DMFT and Cluster-Model Analysis*, Phys. Rev. B **100**, 075146 (2019).

[60] H. Elnaggar, A. Nag, M. W. Haverkort, K.-J. Zhou, and F. de Groot, *Novel Magnetic Excitations beyond the Single- and Double-Magnons*, arXiv:2208.03198.